

## ARTICLE OPEN



# Vital role of magnetocrystalline anisotropy in cubic chiral skyrmion hosts

M. Preißinger<sup>1</sup>✉, K. Karube<sup>2</sup>, D. Ehlers<sup>1</sup>, B. Szigeti<sup>1</sup>, H.-A. Krug von Nidda<sup>1</sup>, J. S. White<sup>3</sup>, V. Ukleev<sup>3</sup>, H. M. Rønnow<sup>4</sup>, Y. Tokunaga<sup>5</sup>, A. Kikkawa<sup>2</sup>, Y. Tokura<sup>2,6</sup>, Y. Taguchi<sup>6</sup> and I. Kézsmárki<sup>1</sup>

Magnetic anisotropy is anticipated to govern the formation of exotic spin textures reported recently in cubic chiral magnets, like low-temperature tilted conical and skyrmion lattice (SkL) states and metastable SkLs with various lattice geometry. Motivated by these findings, we quantified the cubic anisotropy in a series of CoZnMn-type cubic chiral magnets. We found that the strength of anisotropy is highly enhanced towards low temperatures. Moreover, not only the magnitude but also the character of cubic anisotropy drastically varies upon changing the Co/Mn ratio. We correlate these changes with temperature- and composition-induced variations of the helical modulation vectors, deformations of skyrmions, structural rearrangements of the metastable SkLs and the large enhancement of Gilbert damping. Similar studies on magnetic anisotropy are required for the quantitative, unified description of the known stable and metastable modulated spin textures and for the systematic exploration of novel ones in this large class of skyrmion hosts.

npj Quantum Materials (2021)6:65; <https://doi.org/10.1038/s41535-021-00365-y>

## INTRODUCTION

In recent years, magnetic skyrmions have been explored in a great variety of materials, not only in single crystals but also in ultrathin films as well as hetero- and nanostructures<sup>1–9</sup>. Periodic 2D lattices of Bloch-type skyrmions have been first observed in cubic chiral magnets<sup>10–20</sup>. Already in 1976, the archetypical cubic chiral magnet MnSi, in which the formation of a SkL was first reported<sup>10</sup>, had been shown to possess a helimagnetic ground state in zero field<sup>21</sup>, where the  $q$ -vectors of the energetically favoured helical modulations co-align with the magnetocrystalline easy axes, namely the cubic  $\langle 100 \rangle$  axes<sup>22</sup>. In FeGe, another cubic chiral compound hosting Bloch-type SkL nearly up to room temperature<sup>13</sup>, the change of the cubic anisotropy upon cooling was proposed to drive a reorientation of the helical  $q$ -vectors from  $\langle 100 \rangle$  to  $\langle 111 \rangle$  directions<sup>23,24</sup>. In spite of these early observations and the increasing number of theoretical works implying a clear impact of cubic anisotropy on helical spin states<sup>25–36</sup>, the effect of anisotropy on SkLs has only been recognised recently<sup>35,37,38</sup>.

Recently, cubic anisotropy was argued to play an essential role in the formation of a tilted conical and a low-temperature SkL state in Cu<sub>2</sub>OSeO<sub>3</sub><sup>39–41</sup>, another cubic chiral magnet, where a high-temperature SkL state located close to the Curie temperature,  $T_C = 58$  K, was reported earlier<sup>15,18</sup>. This low-temperature SkL forms when the tilted conical state gets destabilised above certain magnetic fields applied along one of the cubic  $\langle 100 \rangle$  axes, being the easy axis of magnetic anisotropy<sup>40,41</sup>. Moreover, in the ultrathin-film form, cubic chiral magnets can also possess an easy-plane anisotropy in addition to the cubic anisotropies. With increasing strength of the easy-plane anisotropy, these systems are predicted to undergo a first-order phase transition from the SkL state into a square vortex-antivortex lattice<sup>42</sup>.

Apart from Bloch-type skyrmions formed by helical spin modulations in cubic chiral helimagnets, skyrmions and

antiskyrmions can also form in crystals with axial symmetry. The lacunar spinels with a polar rhombohedral structure are the first compound family found to host a Néel-type SkL composed of spin cycloids<sup>43</sup>, while the antiskyrmion lattice state was first observed in Heusler compounds with non-centrosymmetric tetragonal structure<sup>44</sup>. In contrast to the small phase pocket of equilibrium SkLs in cubic chiral magnets, these Néel-type skyrmion and antiskyrmion lattices can be stable down to zero temperature<sup>45,46</sup>. In these axially symmetric materials, anisotropy emerges in two forms: (1) the anisotropy of the Dzyaloshinskii–Moriya interaction  $D$  and (2) the uniaxial magnetocrystalline anisotropy. The former confines the magnetic modulation vectors to the plane perpendicular to the unique high-symmetry axis, thereby largely increasing the thermal stability range of the SkL state, while the latter favours collinear states, hence, suppressing modulations<sup>43–50</sup>.

In this study, we quantify the anisotropy and analyse its impact on chiral magnetic states in a series of  $\beta$ -Mn-type (Co<sub>0.5</sub>Zn<sub>0.5</sub>)<sub>20–x</sub>Mn<sub>x</sub> compounds<sup>51</sup>. These materials belong to a family of cubic chiral magnets, hosting skyrmions even well above room temperature<sup>52</sup>. An omnifarious variety of exotic long-periodic magnetic patterns—in addition to the well-known helical, conical and hexagonal SkL—was observed in the Co-Zn-Mn family, including square and rhombic skyrmion lattices<sup>37</sup>, elongated skyrmions<sup>38</sup>, skyrmion chains, meron-antimeron lattices, chiral soliton lattices<sup>53,54</sup>, smectic liquid-crystalline arrangements of skyrmions<sup>55</sup> and domain-wall skyrmions<sup>56</sup>. Similar to Fe<sub>x</sub>Co<sub>1–x</sub>Si<sup>12,16</sup>, their high-temperature equilibrium SkL state can be quenched via field cooling to a metastable state that persists down to low temperatures and can be robust even against the reversal of magnetic field<sup>37,57</sup>. The symmetry of the metastable SkL and the shape of the individual skyrmions show a large variation among these compounds when changing the Co/Mn ratio, which implies a substantial role of cubic anisotropy in determining the internal

<sup>1</sup>Experimental Physics V, Center for Electronic Correlations and Magnetism, Institute of Physics, University of Augsburg, Augsburg, Germany. <sup>2</sup>RIKEN Center for Emergent Matter Science (CEMS), Wako, Saitama, Japan. <sup>3</sup>Laboratory for Neutron Scattering and Imaging (LNS), Paul Scherrer Institute (PSI), Villigen, Switzerland. <sup>4</sup>Laboratory for Quantum Magnetism (LQM), Institute of Physics, École Polytechnique Fédérale de Lausanne (EPFL), Lausanne, Switzerland. <sup>5</sup>Department of Advanced Materials Science, University of Tokyo, Kashiwa, Japan. <sup>6</sup>Department of Applied Physics and Tokyo College, University of Tokyo, Bunkyo-ku, Japan. ✉email: markus.preissinger@physik.uni-augsburg.de

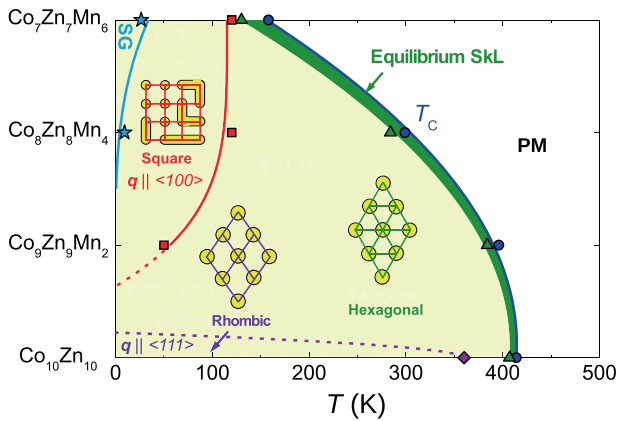


**Fig. 1 Compositional phase diagram.** Schematic phase diagram of the equilibrium and metastable SkLs on the temperature-composition plane for four  $(\text{Co}_{0.5}\text{Zn}_{0.5})_{20-x}\text{Mn}_x$  compounds. Phase boundaries are reproduced from Ref. <sup>54</sup>. The green area indicates the thermodynamically stable SkL pocket below the Curie temperature (blue circles and line). The regime of the metastable SkL phases with pale yellow shading, achieved via a field cooling process <sup>37,38,54</sup>, is separated into four regimes: (1) the transition from the equilibrium SkL into a metastable SkL, preserving the hexagonal symmetry, indicated by green triangles; (2) the crossover from the metastable hexagonal to a metastable square SkL phase in  $\text{Co}_7\text{Zn}_7\text{Mn}_6$ ,  $\text{Co}_8\text{Zn}_8\text{Mn}_4$  and  $\text{Co}_9\text{Zn}_9\text{Mn}_2$ , indicated by red squares, (3) the transformation of the metastable hexagonal into a metastable rhombic SkL state in  $\text{Co}_{10}\text{Zn}_{10}$ , marked by a violet rhombus and (4) the onset of a spin-glass phase (SG) in  $\text{Co}_7\text{Zn}_7\text{Mn}_6$  and  $\text{Co}_8\text{Zn}_8\text{Mn}_4$ , marked by light blue stars. Characteristic temperatures have only been determined for the four compounds and the lines connecting the symbols are to support an easy visualisation.

structure of individual skyrmions and the lattice geometries of these metastable states <sup>38</sup>.

Figure 1 gives an overview of the stable and metastable magnetic phases observed as a function of temperature and composition. Just below the Curie temperature, a small pocket of SkL state emerges in all four target compounds at moderate magnetic fields. Via field cooling this thermodynamically stable hexagonal SkL state can be quenched to lower temperatures. Upon further cooling, in  $\text{Co}_7\text{Zn}_7\text{Mn}_6$ ,  $\text{Co}_8\text{Zn}_8\text{Mn}_4$  and  $\text{Co}_9\text{Zn}_9\text{Mn}_2$ , this metastable SkL gradually transforms into a square lattice <sup>57</sup>. In thin lamellae of  $\text{Co}_8\text{Zn}_8\text{Mn}_4$ , a rectangular arrangement of elongated skyrmions was reported to form, where the elongated skyrmions co-align with the  $\langle 100 \rangle$  cubic axes <sup>38</sup>. In contrast, the metastable SkL in  $\text{Co}_{10}\text{Zn}_{10}$  becomes rhombic with two  $q$ -vectors pointing along the  $\langle 111 \rangle$  axes <sup>54</sup>. At the lowest temperatures, a spin-glass (SG) state emerges in  $\text{Co}_7\text{Zn}_7\text{Mn}_6$  and  $\text{Co}_8\text{Zn}_8\text{Mn}_4$ , where the magnetic modulations are disordered due to frustrated Mn spins <sup>58</sup>.

The stability mechanisms and underlying physics of these exotic spin textures, in particular, the influence of magnetic anisotropy, spin disorder and frustration are far from being understood. In the general model of cubic chiral magnets <sup>29,59</sup>, the wavelength of the chiral magnetic modulations scales with the ratio  $J/D$ , where  $J$  is the isotropic Heisenberg exchange. In addition to equilibrium spin textures, this relation was found to be also applicable for some of the metastable states: micromagnetic simulations have shown that the elongation of skyrmions, leading to a rectangular pattern in  $\text{Co}_8\text{Zn}_8\text{Mn}_4$ , can be reproduced by the decrease of the  $J/D$  ratio in the presence of cubic anisotropy <sup>60</sup>. Easy-axis anisotropy was also suggested to stabilise domain-wall skyrmions <sup>56</sup> and the smectic skyrmion phase <sup>55</sup>. Therefore, measurements of the cubic anisotropy constants in the Co-Zn-Mn alloys are highly desired to correlate theories and experimental observations.

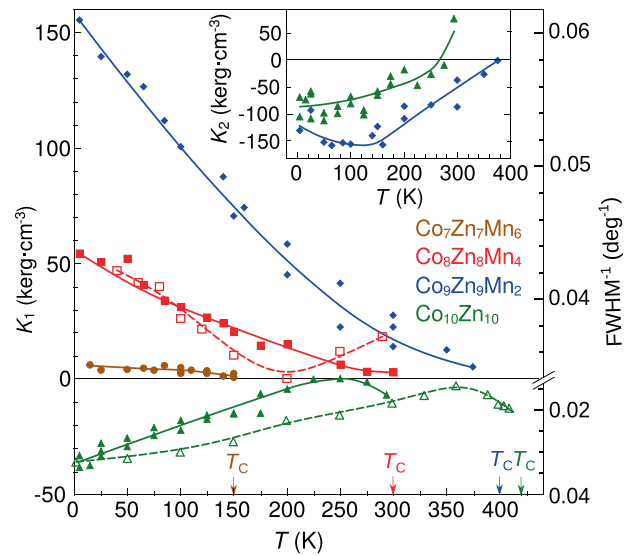


**Fig. 2 Anisotropy constants and modulation length.** Temperature dependence of the cubic anisotropy constants for  $\text{Co}_{10}\text{Zn}_{10}$  (green),  $\text{Co}_9\text{Zn}_9\text{Mn}_2$  (blue),  $\text{Co}_8\text{Zn}_8\text{Mn}_4$  (red) and  $\text{Co}_7\text{Zn}_7\text{Mn}_6$  (brown). The corresponding critical temperatures of the Curie ordering are indicated by arrows. The fourth-order anisotropy constant  $K_1$  (left scale) is indicated by full symbols and with full lines as guides to the eye. The inverse of the full width at half maximum (FWHM) for the SANS intensity peaks (right scale) are plotted by open symbols connected by dashed lines for  $\text{Co}_{10}\text{Zn}_{10}$  (green) and  $\text{Co}_8\text{Zn}_8\text{Mn}_4$  (red). The inset shows the sixth-order anisotropy constant  $K_2$  for  $\text{Co}_{10}\text{Zn}_{10}$  (green) and  $\text{Co}_9\text{Zn}_9\text{Mn}_2$  (blue).

While these examples highlight the importance of magneto-crystalline anisotropy with regard to the stability, symmetry, and shape of individual skyrmions and SkLs, surprisingly, quantitative and systematic experimental studies on the role of anisotropy in cubic skyrmion hosts are virtually non-existing. This provides the main motivation for the present work. Here, using ferromagnetic resonance (FMR) spectroscopy, we investigate the evolution of magnetocrystalline anisotropy in  $(\text{Co}_{0.5}\text{Zn}_{0.5})_{20-x}\text{Mn}_x$  compounds with composition ( $x = 0, 2, 4, 6$ ) and temperature. Moreover, in comparison to the results of small-angle neutron scattering (SANS) experiments, we analyse if changes in anisotropy can account for changes observed in the orientation and the length of the  $q$ -vectors and may eventually lead to transformations between different SkL arrangements. This material class serves as an ideal playground for such investigations, since the material composition can be tuned whilst keeping the cubic chiral symmetry, but vastly changing the ordering temperature, the magnetic properties and—as demonstrated by this work—the strength and nature of cubic anisotropy.

## RESULTS

### Magnetocrystalline anisotropy

Figure 2 summarises the temperature dependence determined from the angular dependence of the FMR of the cubic anisotropy parameters for all the four compounds as described in detail in the Methods. As a common trend, the anisotropy energy decreases with increasing temperature and vanishes smoothly around the Curie temperature, except for  $\text{Co}_{10}\text{Zn}_{10}$ , where the temperature dependence is more complicated. It is important to note that the temperature dependence of the anisotropy energy density is governed by two factors, the temperature dependence of the bare microscopic anisotropies, originating from the spin-orbit coupling, and the temperature dependence of the ordered magnetic moment. Since the latter is saturated in these compounds

typically below  $0.6\text{--}0.8 T_C$ , at lower temperatures the changes in  $K_1$  and  $K_2$  are governed by the variation of the bare anisotropy constants.

Besides its strong thermal variation, the anisotropy is sensitive to the Co/Mn ratio and drastically enhanced with increasing Co content. At low temperatures,  $\text{Co}_8\text{Zn}_8\text{Mn}_4$  and  $\text{Co}_9\text{Zn}_9\text{Mn}_2$  are respectively characterised by  $\sim 10$  and  $\sim 30$  times larger fourth-order cubic anisotropy ( $K_1$ ) than  $\text{Co}_7\text{Zn}_7\text{Mn}_6$ .  $\text{Co}_{10}\text{Zn}_{10}$ , however, does not follow this tendency, instead the  $K_1$  anisotropy term becomes comparatively small in this compound. Increasing Co content also enhances the sixth-order cubic anisotropy ( $K_2$ ). Reduced  $\chi^2$  statistics show that including  $K_2$  does not improve the goodness of the fit in  $\text{Co}_7\text{Zn}_7\text{Mn}_6$  and  $\text{Co}_8\text{Zn}_8\text{Mn}_4$ , on the other hand,  $K_2$  is comparable to  $K_1$  in  $\text{Co}_9\text{Zn}_9\text{Mn}_2$  and even becomes the dominant term in  $\text{Co}_{10}\text{Zn}_{10}$  at low temperatures. In contrast to the strong composition dependence of the anisotropy, the saturation magnetisation per magnetic ion varies by not more than 20% among the four compounds. In terms of the temperature dependence of the anisotropy,  $\text{Co}_{10}\text{Zn}_{10}$  is again an outlier:  $K_1$  approaches zero around 250 K, i.e., well below the Curie temperature, where the  $K_2$  term changes sign.

When the FM state emerges in a cubic crystal, the favoured direction of the magnetic moment is determined by the cubic anisotropy terms given in Eq. (5), assuming the magnetically induced structural distortion is negligible. When  $K_1$  and  $K_2$  are both positive and negative, the easy axes are the  $\langle 100 \rangle$  or  $\langle 111 \rangle$  directions, respectively. The former corresponds to the case of  $\text{Co}_7\text{Zn}_7\text{Mn}_6$  and  $\text{Co}_8\text{Zn}_8\text{Mn}_4$ , while the latter is realised in  $\text{Co}_{10}\text{Zn}_{10}$ . When they have opposite sign, like in  $\text{Co}_9\text{Zn}_9\text{Mn}_2$ , the easy axes are determined by their ratio. Correspondingly,  $\text{Co}_7\text{Zn}_7\text{Mn}_6$ ,  $\text{Co}_8\text{Zn}_8\text{Mn}_4$  and  $\text{Co}_9\text{Zn}_9\text{Mn}_2$  are characterised by easy axes of the magnetisation along the  $\langle 100 \rangle$  directions at all temperatures, though the anisotropy energy is considerably lowered upon approaching the Curie temperature. As an example, the anisotropy energy surface in the FM state of  $\text{Co}_8\text{Zn}_8\text{Mn}_4$  is shown in Fig. 3d, as calculated using the magnetocrystalline anisotropy constants obtained from the fit of  $H_{\text{res}}(\phi)$  in Fig. 3a. This energy surface,  $\mathcal{E}(\mathbf{m})$ , represents the anisotropy of the FM state or equivalently the anisotropy experienced by an individual spin.

For a more complex magnetic texture, like the helical spin order, the magnetic anisotropy energy has to be evaluated for the whole magnetic unit cell, i.e., by summing over all spins in one period of the helix. Correspondingly, for a helix, where the  $q$ -vector is perpendicular to the spin rotation plane, the dependence of the magnetic energy on the orientation of the  $q$ -vector,  $\mathcal{E}(\mathbf{q})$ , can be obtained by averaging the anisotropy energy of a single spin for all directions of  $\mathbf{m}$  in the plane perpendicular to the  $q$ -vector. (In this simple approach, we treat the magnetic modulations as fully harmonic spin helices and disregard possible effects of anharmonicity.) When the magnetic easy axes are the  $\langle 100 \rangle$  directions, as is the case in  $\text{Co}_8\text{Zn}_8\text{Mn}_4$ , the preferred  $q$ -vectors also point along the  $\langle 100 \rangle$  axes. In fact, the shapes of the two energy surfaces,  $\mathcal{E}(\mathbf{m})$  and  $\mathcal{E}(\mathbf{q})$ , are rather similar, as clear from Fig. 3d, g. Qualitatively, the same scenario applies also for  $\text{Co}_7\text{Zn}_7\text{Mn}_6$  and  $\text{Co}_9\text{Zn}_9\text{Mn}_2$ , though the weaker/stronger anisotropy in the former/latter case leads to more spherical/rectangular energy surfaces compared to  $\text{Co}_8\text{Zn}_8\text{Mn}_4$ .

In contrast, the magnetic easy axes point along the  $\langle 111 \rangle$  directions in  $\text{Co}_{10}\text{Zn}_{10}$  at low temperatures, as clear from Fig. 3e. Although the helical modulation vectors also favour the  $\langle 111 \rangle$  directions, the two energy surfaces,  $\mathcal{E}(\mathbf{m})$  and  $\mathcal{E}(\mathbf{q})$ , are quite different and  $q$ -vectors between  $\langle 111 \rangle$  and  $\langle 110 \rangle$  axes have nearly the same energy. Only the  $\langle 100 \rangle$  axes are clearly distinguished as unfavoured directions, as can be traced in Fig. 3h. Moreover, with increasing temperature, both anisotropy terms weaken strongly and  $K_2$  even changes sign at  $\sim 250$  K. Consequently, the  $\langle 100 \rangle$  directions, being the hard axes of

magnetisation at low-temperatures, nearly become the easy axes [Fig. 3f]. In this temperature range, the eighth-order anisotropy constant  $K_3$  ( $K_3 \approx 23$  kerg) becomes the dominant anisotropy term and defines the location of the shallow energy minima in the vicinity of the  $\langle 100 \rangle$  axes. Interestingly, at these temperatures, the favoured  $q$ -vectors do not point along any of the high-symmetry directions, instead they are located around circles centred at  $\langle 100 \rangle$  axes. In that regions, a Mexican hat-like form of  $\mathcal{E}(\mathbf{q})$  can be discerned in Fig. 3i.

### Magnetic modulations and anisotropy

In the following, we perform a comparative analysis of FMR and SANS data to reveal how the variation of cubic anisotropy with temperature and composition affects the magnetic modulations in this series of  $(\text{Co}_{0.5}\text{Zn}_{0.5})_{20-x}\text{Mn}_x$  compounds. The SANS data are reproduced from Refs. <sup>37,54</sup> and re-analysed here to gain more insight into the angular distribution of the  $q$ -vectors. At low temperatures, the SANS intensity is confined to the  $\langle 100 \rangle$  directions in  $\text{Co}_9\text{Zn}_9\text{Mn}_2$ ,  $\text{Co}_8\text{Zn}_8\text{Mn}_4$  and  $\text{Co}_7\text{Zn}_7\text{Mn}_6$ , i.e., the helical  $q$ -vectors favour these directions, as exemplified by the SANS image in Fig. 4a, recorded in the (001) plane for  $\text{Co}_8\text{Zn}_8\text{Mn}_4$ . In contrast, in the SANS intensity of  $\text{Co}_{10}\text{Zn}_{10}$ , displayed over the (110) plane in Fig. 4b, the maxima are located at the  $\langle 111 \rangle$  directions at low temperatures. (In both materials, the difference in the intensity of symmetry-equivalent  $q$ -vectors originates from unequal population of the corresponding helical domains.)

The angular distribution of the  $q$ -vectors becomes broader with increasing temperature in both materials, as clear from the increase of the full width at half maximum (FWHM) for the SANS intensity maxima, plotted in Fig. 2. While in  $\text{Co}_{10}\text{Zn}_{10}$ , the FWHM is more than doubled ( $31^\circ \rightarrow 71^\circ$ ) between 5 and 370 K, it is only increased by about 20% ( $23^\circ \rightarrow 29^\circ$ ) in  $\text{Co}_8\text{Zn}_8\text{Mn}_4$  between 50 and 200 K. In fact, the inverse of the FWHM follows a temperature dependence similar to that of the  $K_1$  values. This shows that the anisotropy does not only select the favoured orientation of the  $q$ -vectors but also controls their spread around the preferred directions. In addition to the enhanced orientational disorder of the  $q$ -vectors towards higher temperatures, in  $\text{Co}_{10}\text{Zn}_{10}$  between 250 and 410 K, the favoured  $q$ -vectors move away from the  $\langle 111 \rangle$  to  $\langle 100 \rangle$  directions, as expected from the temperature-induced changes in  $\mathcal{E}(\mathbf{q})$  and can be traced well in Fig. 4c.

Since apparently the helical  $q$ -vectors arrange in a way to minimise the anisotropy energy, in Fig. 4d–f, we directly compare the angular dependence of the SANS intensity and  $\mathcal{E}(\mathbf{q})$ . In  $\text{Co}_8\text{Zn}_8\text{Mn}_4$ ,  $\mathcal{E}(\mathbf{q})$  has minima along the  $\langle 100 \rangle$  axes, coinciding with the SANS intensity maxima [Fig. 3d]. In  $\text{Co}_{10}\text{Zn}_{10}$ , a similar confinement of the  $q$ -vectors by anisotropy is observed around the  $\langle 111 \rangle$  axes at low temperature, though the width of the SANS intensity maxima are considerably broader due to the weaker anisotropy in this compound [Fig. 4e]. Note that  $\mathcal{E}(\mathbf{q})$  only shows little dependence in the range of  $[\bar{1}\bar{1}\bar{1}]$ – $[\bar{1}\bar{1}0]$ – $[\bar{1}11]$ . At higher temperatures, this dependence is getting even weaker with an overall change in  $\mathcal{E}(\mathbf{q})$  at 250 K approx.  $2 \text{ kerg} \cdot \text{cm}^{-3}$ , compared to  $15 \text{ kerg} \cdot \text{cm}^{-3}$  at 50 K. Consequently, though the global minima are located around circles centred at  $\langle 100 \rangle$  axes, as shown in Fig. 3i, due to the weakness of anisotropy the helical  $q$ -vectors can get pinned along arbitrary directions, as clear from the 250 K data in Fig. 4f. The close correlation between minima of  $\mathcal{E}(\mathbf{q})$  and maxima of the SANS intensity is observed at 410 K.

### Magnetic modulations and gilbert damping

At the Curie temperature, the Gilbert-damping parameter  $\alpha$  of these compounds ranges from 0.04 to 0.05, which is typical for ferromagnetic cobalt. Upon cooling,  $\alpha$  is enhanced in all the four compounds; however, the strength of the increase depends strongly on the Co/Mn ratio, as clear from Fig. 5. It is nearly tripled in  $\text{Co}_7\text{Zn}_7\text{Mn}_6$ , while it increases only by  $\sim 50\%$  in  $\text{Co}_{10}\text{Zn}_{10}$ .

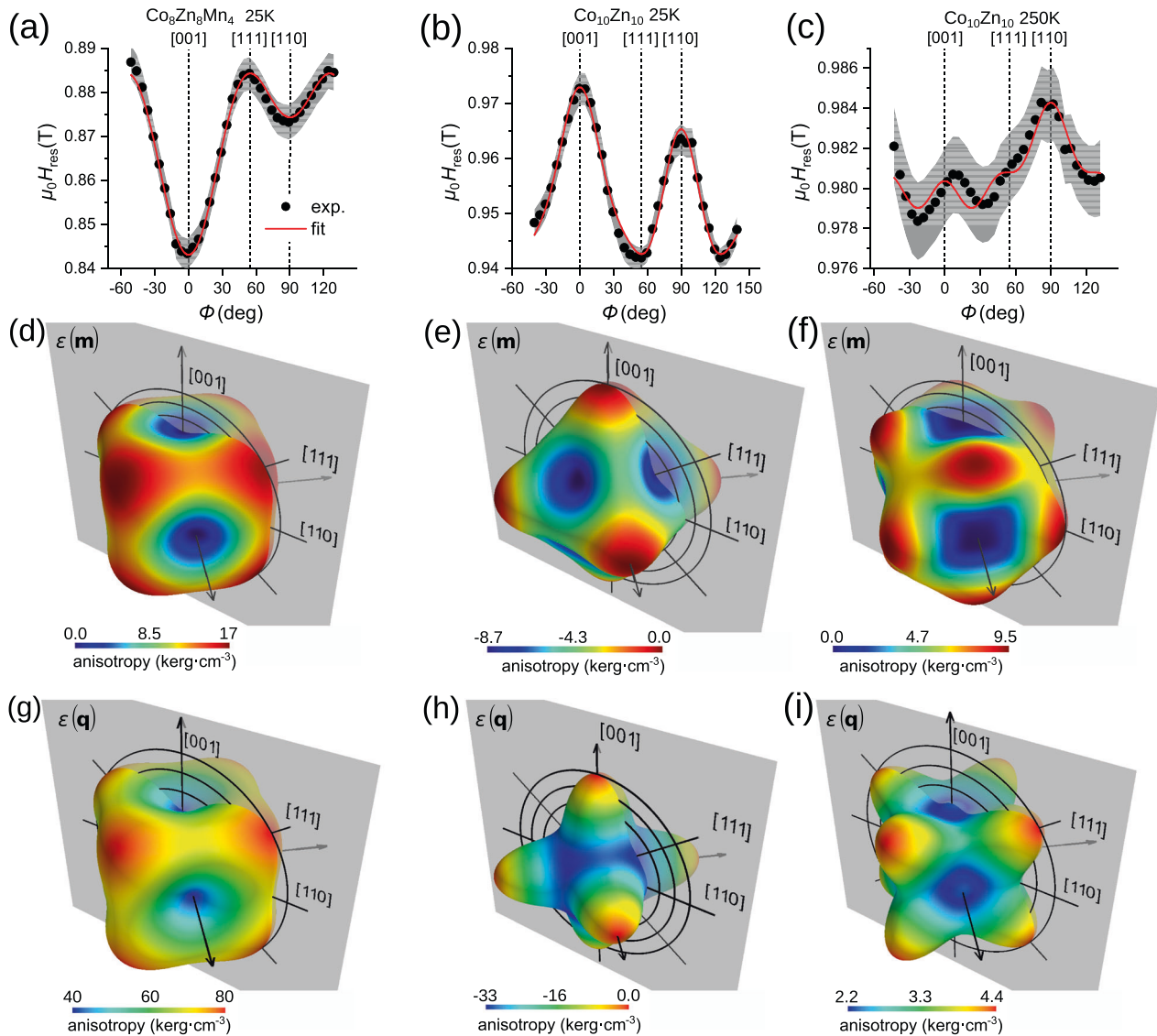


**Fig. 3 Anisotropy surfaces.** Angular dependence of the ferromagnetic resonance field,  $H_{res}$ , in the  $(\bar{1}\bar{1}0)$  plane is shown in **a** for  $\text{Co}_8\text{Zn}_8\text{Mn}_4$  at 25 K and in **b** and **c** for  $\text{Co}_{10}\text{Zn}_{10}$  at 25 and 250 K, respectively. Black dots are the experimental data points, representing the resonance fields as fitted from the individual spectra that were recorded in  $5^\circ$  steps during a rotation of the magnetic field within the  $(\bar{1}\bar{1}0)$ -plane, as sketched in Fig. 6. Red lines show the fit of the magnetocrystalline anisotropy using Eqs. (4) and (5). The error of the resonance field (grey coloured area) was estimated to be 5% of the linewidth of the resonance peak. **d–f** display the anisotropy energy surface of the ferromagnetic state,  $\mathcal{E}(\mathbf{m})$ , calculated based on the  $K_1$ ,  $K_2$  and  $K_3$  values obtained from the fits in the corresponding panels above. **g–i** show the anisotropy energy of the helical state versus the orientation of the  $q$ -vector,  $\mathcal{E}(\mathbf{q})$ , again calculated using the parameters obtained in the corresponding top panels. Arrows in panels **d–i** indicate the  $\langle 100 \rangle$  axes. In the rotation plane of the magnetic field, the grey  $(\bar{1}\bar{1}0)$  plane,  $\langle 111 \rangle$  and  $\langle 110 \rangle$  axes are also shown.

Surprisingly,  $a$  and the length of the  $q$ -vectors show quantitatively similar thermal variations in all compounds except for  $\text{Co}_{10}\text{Zn}_{10}$ : They are both constant through the thermodynamically stable as well as the metastable hexagonal SKL phases, but exhibit a sudden uprise associated with the transformation from the metastable hexagonal to the square lattice phase. On the other hand,  $a$  and the FWHM of the  $q$ -vectors do not show a similar temperature dependence. Instead, the temperature dependence of the latter is reminiscent of that of  $K_1$ , as seen in Fig. 2 and discussed earlier.

The strikingly similar temperature dependences of the  $q$ -vector length and the Gilbert damping imply a common underlying microscopic mechanism. A possible scenario is that antiferromagnetic correlations of Mn spins developing towards low temperatures weaken the ferromagnetic exchange ( $J$ ) without significantly affecting the Dzyaloshinskii–Moriya interaction ( $D$ ) between Co

spins and, hence, increase the length of the  $q$ -vectors according to  $|\mathbf{q}| \propto D/J$ . This also explains why the increase of  $|\mathbf{q}|$  starts at a lower temperature in  $\text{Co}_9\text{Zn}_9\text{Mn}_2$  with higher Co content than in  $\text{Co}_8\text{Zn}_8\text{Mn}_4$  and  $\text{Co}_7\text{Zn}_7\text{Mn}_6$ , despite  $K_1$  being larger in  $\text{Co}_9\text{Zn}_9\text{Mn}_2$  than in  $\text{Co}_8\text{Zn}_8\text{Mn}_4$  and  $\text{Co}_7\text{Zn}_7\text{Mn}_6$ . In this picture, the low-temperature enhancement of Gilbert damping is governed by static or dynamic disorder of Mn spins, since the Co spins are fully spin polarised in magnetic fields above 1 T, where  $a$  was determined from the FMR spectra. Thus, the parallel increase of  $|\mathbf{q}|$  and  $a$  observed towards low temperatures can be naturally explained by the suppression of  $J$  due to increasing antiferromagnetic correlations between Mn spins. Geometrical frustration of the Mn spins occupying 8c Wyckoff positions at Mn concentrations above  $x=4$  was reported to drive the formation of a SG ground state<sup>61</sup>. A drop in  $a$  is found below the onset of the

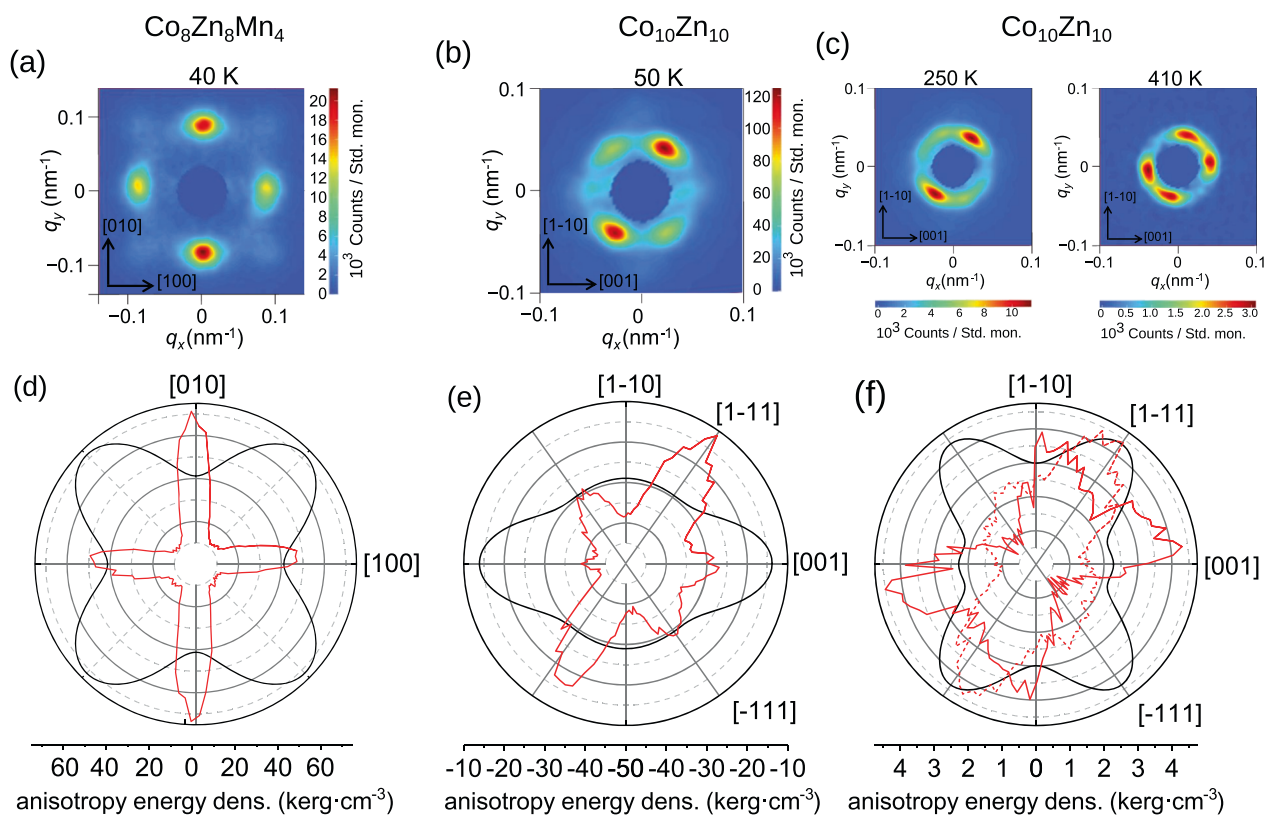


**Fig. 4**  $q$ -vector anisotropy. **a** SANS intensity of  $\text{Co}_8\text{Zn}_8\text{Mn}_4$  recorded in the (001) plane at 40 K. and of  $\text{Co}_{10}\text{Zn}_{10}$  in the (110) plane at **b** 50 K and **c** 250 and 410 K. Direct comparison between the dependence of the magnetocrystalline anisotropy energy of the helix (black curves) and the SANS intensity (red curves) upon rotation in the (100)-plane for  $\text{Co}_8\text{Zn}_8\text{Mn}_4$  at 40 K (**d**) and for  $\text{Co}_{10}\text{Zn}_{10}$  upon rotation in the (110) plane at 50 K (**e**) as well as 250 K (dashed curve) and 410 K (solid curve) (**f**). In panels **d–f**, the anisotropy energy curves are the corresponding cross-sections of the anisotropy energy surfaces in Fig. 3g–i, while the angular-dependent SANS intensity curves are obtained by radial averaging of the SANS intensities in panels **a–c**.

SG phase [see Fig. 5a, b], as observed in canonical SG materials<sup>62</sup>. Again,  $\text{Co}_{10}\text{Zn}_{10}$  is an outlier where both  $\alpha$  and  $|\mathbf{q}|$  exhibit little temperature dependence with no clear correlation between the two.

## DISCUSSION

In the present work, we studied the evolution of the cubic anisotropy in a series of  $(\text{Co}_{0.5}\text{Zn}_{0.5})_{20-x}\text{Mn}_x$  cubic chiral magnets with octahedral (O) symmetry. While these compounds are isostructural and the magnitude of the saturated magnetic moment does not vary by more than 20% upon changing the Co/Mn ratio, the magnetic interactions show a strong dependence on the composition, as already reflected by the large variation of the Curie temperature between 150 and 410 K. Here we show that this series offers an excellent laboratory to study the effects of anisotropy on chiral spin textures. This is because not only the magnitude of the anisotropy shows drastic variation with the Co/Mn ratio and the temperature, but also the character of the anisotropy changes, as reflected by the reorientation of the easy axes from  $\langle 100 \rangle$  to  $\langle 111 \rangle$  directions with increasing Co content.

The fourth-order and—when relevant—also the sixth-order cubic anisotropies weaken towards higher temperatures in all these compounds. Remarkably, the eighth-order anisotropy also comes into play in  $\text{Co}_{10}\text{Zn}_{10}$  near room temperature, due to the weakness of the lower-order terms. As a consequence, the helical  $q$ -vectors in this compound experience a Mexican hat-like potential centred around the  $\langle 100 \rangle$  directions. A similar deviation of the favoured  $q$ -vectors from high-symmetry directions has been reported in Co/Fe-doped MnSi, though in that case the effect

originates from a competition of fourth- and sixth-order anisotropies allowed by the tetrahedral cubic (T) symmetry<sup>63</sup>. We found that the cubic anisotropy terms do not only select the favoured orientation of the  $q$ -vectors in the helical state but also control the width of their angular distribution around the preferred directions. Correspondingly, the suppression of magnetic anisotropy towards higher temperatures leads to an increasing orientational disorder of the helical  $q$ -vectors.

Besides defining the orientation of the  $q$ -vectors of the equilibrium chiral spin states, the anisotropy also plays a role in the transformation of metastable hexagonal SkL to square or rhombic lattices. In these compounds, the  $D/J$  ratio increases with lowering the temperature, as reflected by the elongation of the  $q$ -vectors upon cooling. Correspondingly, the originally close-packed hexagonal arrangement of skyrmions within the metastable SkLs becomes loose towards low temperatures, due to the conservation of the skyrmion number. Releasing the close-packing constraint leads to anisotropy-controlled rearrangements of the metastable skyrmions. In  $\text{Co}_9\text{Zn}_9\text{Mn}_2$ ,  $\text{Co}_8\text{Zn}_8\text{Mn}_4$  and  $\text{Co}_7\text{Zn}_7\text{Mn}_6$  a square lattice or a rectangular arrangement of elongated skyrmions forms with  $q$ -vectors along the  $\langle 100 \rangle$  easy directions. In the rectangular arrangement, observed by real-space imaging in thin samples, the skyrmions are forced to elongate parallel to the magnetic easy axes. Interestingly, the Gilbert damping shows a temperature dependence similar to  $|\mathbf{q}|$ , thus, can be used to locate these transitions.

The anisotropy plays an even more important role in the distortion of the metastable hexagonal SkL in  $\text{Co}_{10}\text{Zn}_{10}$ . In the other three compounds, the change in  $D/J$  determines the temperature range where the hexagonal to square lattice transition takes place

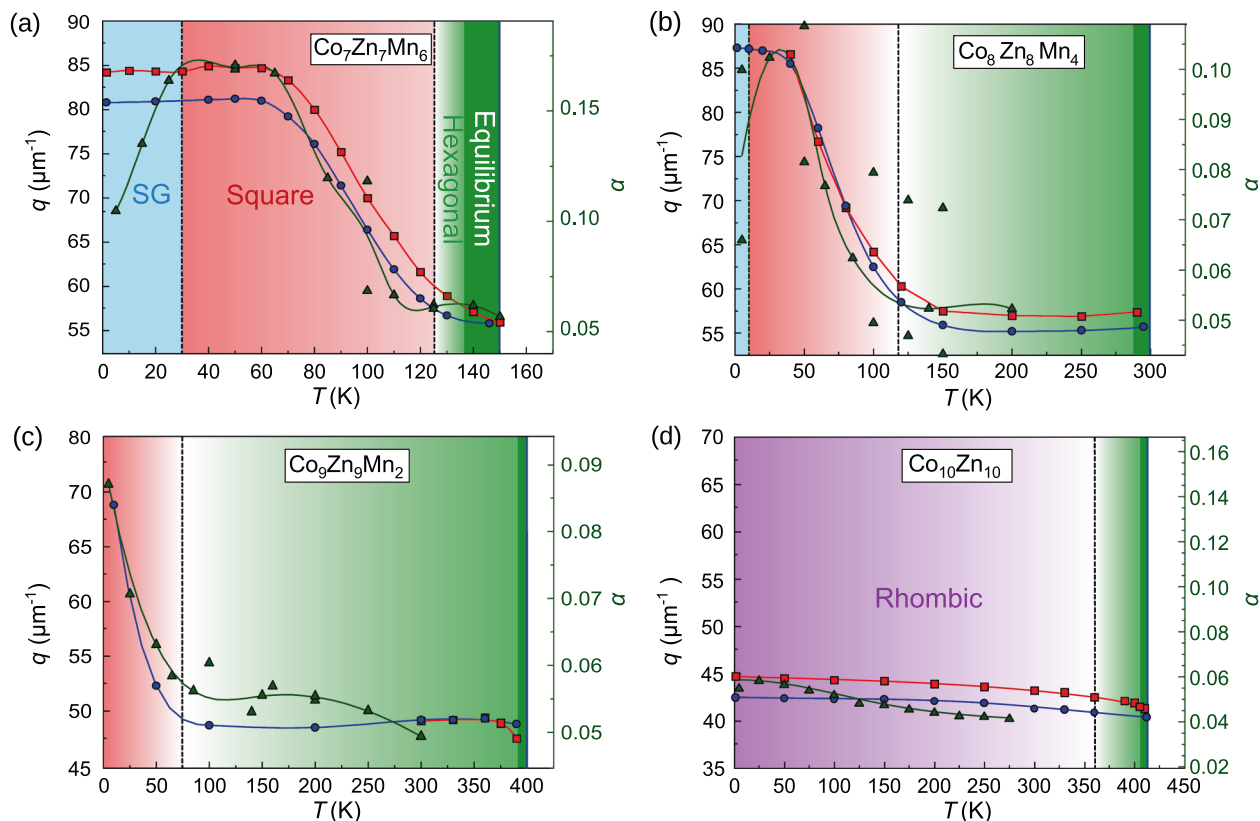


**Fig. 5 Magnetic modulations and damping.** Comparison between the temperature dependence of the length of the  $q$ -vectors (left scale) and the Gilbert-damping parameter  $a$  (right scale) in the metastable SkLs of **a**  $\text{Co}_7\text{Zn}_7\text{Mn}_6$ , **b**  $\text{Co}_8\text{Zn}_8\text{Mn}_4$ , **c**  $\text{Co}_9\text{Zn}_9\text{Mn}_2$  and **d**  $\text{Co}_{10}\text{Zn}_{10}$ . Blue circles show the  $q$ -vector length in the SkL states, obtained during field cooling, and red squares in the helical phase, while green triangles indicate  $a$ . The green area represents the equilibrium SkL state just below the Curie temperature (blue line). The green shaded area represents the regime over which the metastable SkL preserves the hexagonal symmetry, while the red and violet shaded areas indicate the square and rhombic SkL states, respectively. The light blue shaded area stands for the spin-glass phase (see also Fig. 1).

and the anisotropy only governs the type of the distortion. This hierarchy is clear from the fact that the transition temperatures do not correlate with the magnitudes of the anisotropy for  $\text{Co}_9\text{Zn}_9\text{Mn}_2$ ,  $\text{Co}_8\text{Zn}_8\text{Mn}_4$  and  $\text{Co}_7\text{Zn}_7\text{Mn}_6$ . In contrast, the length of the  $q$ -vectors shows very weak temperature dependence in  $\text{Co}_{10}\text{Zn}_{10}$  compared to the other compounds. Still, the distortion of the metastable hexagonal SkL to a rhombic lattice with  $q$ -vectors along the  $\langle 111 \rangle$  easy directions takes place at the highest temperature. This is likely because the rearrangement into the rhombic SkL requires a smaller distortion than to the square-lattice form and can be driven by the anisotropy.

Finally, we discuss why an anisotropy-driven low-temperature equilibrium SkL—like the one observed in  $\text{Cu}_2\text{OSeO}_3$ —does not emerge in  $\text{Co}_7\text{Zn}_7\text{Mn}_6$ ,  $\text{Co}_8\text{Zn}_8\text{Mn}_4$ ,  $\text{Co}_9\text{Zn}_9\text{Mn}_2$ , though all four compounds have magnetic easy axes along the  $\langle 100 \rangle$  directions. (Though in  $\text{Co}_7\text{Zn}_7\text{Mn}_6$  a low-temperature equilibrium SkL has been observed, it forms due to magnetic frustration and is not stabilised by cubic anisotropy<sup>58</sup>.) According to the theory in Ref.<sup>39</sup>, the low-temperature SkL can emerge for magnetic fields applied along the  $\langle 100 \rangle$  directions, if  $K_1$  exceeds the critical value of  $K_c = 0.07 \mu_0 H_{c2} M_s$ , where  $H_{c2}$  is the critical field separating the conical and the field-polarised states and  $M_s$  is the saturation magnetisation. The estimated  $K_c$  values, based on the saturation magnetisation and critical field values obtained in previous works<sup>54,64</sup>, are  $K_c = 27 \text{ kerg} \cdot \text{cm}^{-3}$  for  $\text{Co}_7\text{Zn}_7\text{Mn}_6$ ,  $K_c = 113 \text{ kerg} \cdot \text{cm}^{-3}$  for  $\text{Co}_8\text{Zn}_8\text{Mn}_4$  and  $K_c = 132 \text{ kerg} \cdot \text{cm}^{-3}$  for  $\text{Co}_9\text{Zn}_9\text{Mn}_2$ . For the first two,  $K_1$  is somewhat below the critical value needed to stabilise the low-temperature SkL. Though  $K_1$  is somewhat larger than the critical value in  $\text{Co}_9\text{Zn}_9\text{Mn}_2$  at low temperatures, its effect is weakened by the large  $K_2$  of opposite sign. This explains why the

low-temperature SkL is not realised in this Co-Zn-Mn series, though the absolute values of  $K_1$  determined for  $\text{Co}_8\text{Zn}_8\text{Mn}_4$  and  $\text{Co}_9\text{Zn}_9\text{Mn}_2$  are orders of magnitude higher than in  $\text{Cu}_2\text{OSeO}_3$ ,  $K_1 = 6 \text{ kerg} \cdot \text{cm}^{-3}$ <sup>65</sup>.

In conclusion, we believe that our work, demonstrating how the quantitative determination of anisotropy terms can promote the understanding of complex spin states and related phenomena, will trigger similar experimental studies as well as theoretical approaches accounting for the effects of magnetic anisotropy on the properties of chiral magnets.

## METHODS

### Ferromagnetic resonance

In order to determine the magnetocrystalline anisotropy energy, we studied the angular dependence of the FMR field in the field-polarised ferromagnetic state of  $(\text{Co}_{0.5}\text{Zn}_{0.5})_{20-x}\text{Mn}_x$  with  $x = 0, 2, 4, 6$  at temperatures ranging from 4 to 400 K. Single crystals of  $\text{Co}_{10}\text{Zn}_{10}$  were grown by a self-flux method from pure Co and Zn sealed in an evacuated quartz tube. Single crystals of  $\text{Co}_9\text{Zn}_9\text{Mn}_2$ ,  $\text{Co}_8\text{Zn}_8\text{Mn}_4$  and  $\text{Co}_7\text{Zn}_7\text{Mn}_6$  were grown by the Bridgman method from pure Co, Zn and Mn sealed in an evacuated quartz tube. The specimens were  $\{110\}$  cuts of single crystals polished to a cylindrical disc-form with a typical diameter of  $\sim 1 \text{ mm}$  and thickness of  $\sim 200 \mu\text{m}$ . Field-swept FMR spectra were recorded at two different frequencies, X-band (9.4 GHz) and Q-band (34 GHz), in  $5^\circ$  steps upon rotation of the magnetic field in the  $(1\bar{1}0)$  plane. Since the field-polarised ferromagnetic state has already been achieved at 1 kOe in all the four compounds irrespective of the temperature, the FMR line, located always above 3 kOe, does not overlap with either the collective modes of the modulated states or spectral features related to metamagnetic transitions.

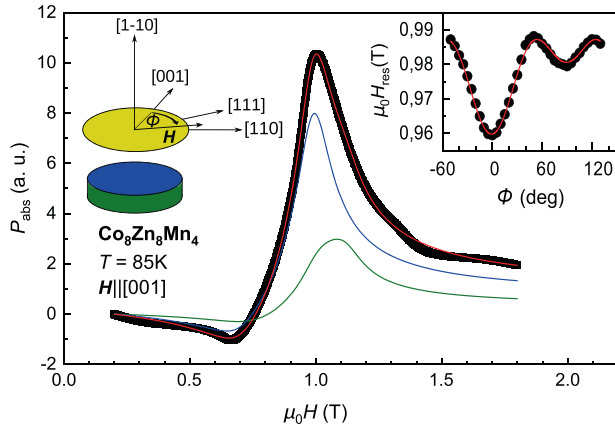


**Fig. 6 Field-swept FMR spectrum.** Field-swept FMR (microwave absorption) spectrum of  $\text{Co}_8\text{Zn}_8\text{Mn}_4$  recorded at 85 K with magnetic field along the [001] axis. The spectrum can be decomposed into two parts: a sharp resonance (blue line) originating from the top and bottom face of the sample and a broader peak (green line) coming from the mantle, as sketched with corresponding colours in the top-left corner. The dependence of the resonance field on  $\phi$  is shown in the inset, where  $\phi$  is the angle spanned by the field and the [001] axis upon rotation of the magnetic field within the  $(1\bar{1}0)$  plane. The field rotation plane, indicated as a pale yellow disk in the top-left corner, is parallel to the top and bottom surface of the sample.

The FMR spectra, see Fig. 6 for a representative field-dependent microwave absorption spectrum, were reproduced and the resonance fields,  $H_{\text{res}}$ , determined using the Landau–Lifshitz–Gilbert equation<sup>66,67</sup>

$$\frac{d\mathbf{M}}{dt} = -\gamma\mathbf{M} \times \mathbf{H} - \gamma \frac{\alpha}{M_s} \mathbf{M} \times \frac{d\mathbf{M}}{dt}, \quad (1)$$

where  $\mathbf{M} = (m_x, m_y, M_0)$  is the time-dependent magnetisation,  $M_s$  the saturation magnetisation,  $\gamma$  the gyromagnetic ratio and  $\mathbf{H} = (h_x, h_y, H_0)$  the applied magnetic field. The microwave field rotates in the  $xy$  plane, while the static magnetic field, causing the Larmor precession is swept adiabatically in  $z$  direction. Using  $M_{\pm} = M_x + iM_y$  and  $H_{\pm} = H_x + iH_y$ , the absorbed microwave power  $P_{\text{abs}} = \sqrt{|\mu_{\pm}|} - \text{Im} \mu$  is derived from the permeability

$$\mu_{\pm} = 1 + \frac{4\pi M_{\pm}}{H_{\pm}} = 1 + \frac{4\pi M_0}{H_0 - \frac{\omega}{\gamma} + i\alpha\omega}. \quad (2)$$

Besides  $H_{\text{res}} = \omega/\gamma$ , the Gilbert-damping parameter  $\alpha$  and the magnetisation were also extracted from the fit. For all samples, the latter showed good agreement with magnetisation data measured directly by SQUID (Supplementary Fig. 1).

Due to the skin effect characteristic of such metallic samples, the magnetisation dynamics can be described by the thin-film variant of the Kittel formula<sup>68</sup>

$$\frac{\omega}{\gamma} = H_{\text{res}} = \sqrt{H_i [H_i + 4\pi M \cdot \sin^2(\theta)]}, \quad (3)$$

where  $\theta$  is the angle between the magnetisation and the surface normal of the metallic specimen,  $H_{\text{res}}$  the resonance field and  $H_i$  the magnetic field inside the specimen, which has been reduced by the demagnetisation field  $H_{\text{dem}} = (N_x - N_z)M$ . The static magnetic field penetrates the entire specimen, while only a thin surface layer of the metallic specimen contributes to the microwave absorption. Due to the geometry of the samples, the coupling of the surface layer to the internal magnetisation of the specimen depends on  $\theta$ . Consequently, the main resonance peak from the top and the bottom of the specimen is shifted with respect to the resonance originating from the mantle of the cylindrical sample. Since the demagnetisation varies with  $\theta$  around the mantle, the resonance field changes accordingly, leading to a second broader peak partially overlapping with the main peak. In addition, a dip at the left side of the main resonance is expected to appear, related to the so-called antiresonance<sup>69–71</sup>. Its onset and width are controlled by the magnetisation, while the Gilbert damping determines the linewidth of the main peak without capturing this dip.

Our analysis based on Eqs (2) and (3) could reproduce all features of the field-swept FMR spectra, as shown in Fig. 6, thus, facilitated a precise

determination of  $\alpha$  and  $H_{\text{res}}(\phi)$ , where  $\phi$  is the angle spanned by the [001] axis and the magnetic field upon the rotation of the field in the  $(1\bar{1}0)$  plane. Due to the cylindrical sample shape, the angular dependence of  $H_{\text{res}}$  is solely governed by the cubic anisotropy. We determined the cubic anisotropy parameters,  $K_1$  and  $K_2$  from a fitting routine based on the Smit–Suhl formula<sup>72,73</sup>:

$$H_{\text{res}} = \frac{1}{m \sin \theta} \sqrt{\frac{\partial^2 \mathcal{E}}{\partial \theta^2} \Big|_0 \frac{\partial^2 \mathcal{E}}{\partial \phi^2} \Big|_0 - \left( \frac{\partial^2 \mathcal{E}}{\partial \theta \partial \phi} \Big|_0 \right)^2}, \quad (4)$$

where

$$\mathcal{E} = -\mathbf{M}\mathbf{H} + K_1 (m_x^2 m_y^2 + m_x^2 m_z^2 + m_y^2 m_z^2) + K_2 m_x^2 m_y^2 m_z^2 + K_3 (m_x^2 m_y^2 + m_y^2 m_z^2 + m_z^2 m_x^2) \quad (5)$$

is the free energy, including the Zeeman term as well as fourth-order ( $K_1$ ), sixth-order ( $K_2$ ) and eighth-order ( $K_3$ ) cubic anisotropy terms with  $m_x$ ,  $m_y$  and  $m_z$  being the direction cosines of the magnetisation, while  $\theta$  and  $\phi$  are the polar and azimuthal angles. The value of the magnetisation was taken from SQUID measurements performed at 1 T, close to the FMR (Supplementary Fig. 1). In the FMR setup, the magnetic field rotates in the (011) plane, i.e., magnetisation and field are given by

$$\begin{aligned} \frac{\mathbf{M}}{M_0}, \frac{\mathbf{H}}{H_0} = & \sin(\theta, \theta_H) \cos(\phi, \phi_H) \cdot \mathbf{e}_x + \\ & + \frac{\sqrt{2}}{2} (\cos(\theta, \theta_H) + \sin(\theta, \theta_H) \sin(\phi, \phi_H)) \cdot \mathbf{e}_y + \\ & + \frac{\sqrt{2}}{2} (\cos(\theta, \theta_H) - \sin(\theta, \theta_H) \sin(\phi, \phi_H)) \cdot \mathbf{e}_z. \end{aligned} \quad (6)$$

Here,  $\phi$  and  $\phi_H$  are the azimuthal angles between the crystallographic  $x$ -axis and the projection of the magnetisation and field into the  $xy$  plane and  $\theta$  and  $\theta_H$  are the polar angles between the crystallographic  $z$ -axis and the magnetisation and field. Examples of  $H_{\text{res}}(\phi)$  curves and the corresponding fits are displayed in the inset of Figs. 6 and 3a–c for  $\text{Co}_8\text{Zn}_8\text{Mn}_4$  at low temperature and for  $\text{Co}_{10}\text{Zn}_{10}$  both at low and near room temperature.

### Small-angle-neutron scattering

In order to correlate changes of the anisotropy with transformations of the magnetic modulations, we also present SANS data for  $\text{Co}_8\text{Zn}_8\text{Mn}_4$  and  $\text{Co}_{10}\text{Zn}_{10}$  that are reproduced from previous works<sup>37,54</sup>. SANS images were recorded in the (100) plane for  $\text{Co}_8\text{Zn}_8\text{Mn}_4$  and in the (110) plane for  $\text{Co}_{10}\text{Zn}_{10}$ . The SANS measurements were performed at the SANS-I instrument in the Paul Scherrer Institute for  $\text{Co}_{10}\text{Zn}_{10}$ ,  $\text{Co}_9\text{Zn}_9\text{Mn}_2$  and  $\text{Co}_8\text{Zn}_8\text{Mn}_4$ , and at the D33 instrument in the Institute Laue-Langevin for  $\text{Co}_7\text{Zn}_7\text{Mn}_6$ . The neutron wavelength was selected to be 10 Ångström. SANS intensities on the reciprocal  $q_x q_y$  plane were obtained summing the multiple data taken over rocking scans by subtracting nuclear and instrumental background signals. To determine the orientation of the favoured  $q$ -vectors, the angular dependence of the SANS intensity has been fitted with Gaussian peaks. The width of peaks corresponding to symmetry-equivalent directions has been averaged. In addition, we also compare the temperature dependence of Gilbert damping and the length of the  $q$ -vectors,  $|q|$ , for all the four compounds, the latter reproduced from Ref.<sup>54</sup>.

### DATA AVAILABILITY

The data sets measured and analysed for the current study are available from the corresponding author upon reasonable request.

Received: 15 January 2021; Accepted: 12 June 2021;

Published online: 07 July 2021

### REFERENCES

- Heinze, S. et al. Spontaneous atomic-scale magnetic skyrmion lattice in two dimensions. *Nat. Phys.* **7**, 713–718 (2011).
- Wilson, M. N. et al. Extended elliptic skyrmion gratings in epitaxial MnSi thin films. *Phys. Rev. B* **86**, 144420 (2012).
- Yu, X., DeGrave, J. P., Hara, Y., Hara, T., Jin, S. & Tokura, Y. Observation of the magnetic skyrmion lattice in a MnSi nanowire by Lorentz TEM. *Nano Lett.* **13**, 3755–3759 (2013).
- Du, H. et al. Electrical probing of field-driven cascading quantized transitions of skyrmion cluster states in MnSi nanowires. *Nat. Commun.* **6**, 7637 (2015).

5. Moreau-Luchaire, C. et al. Additive interfacial chiral interaction in multilayers for stabilization of small individual skyrmions at room temperature. *Nat. Nanotech.* **11**, 444–448 (2016).
6. Stolt, M. J. et al. Selective chemical vapor deposition growth of cubic FeGe nanowires that support stabilized magnetic skyrmions. *Nano Lett.* **17**, 508–514 (2017).
7. Hervé, M. et al. Stabilizing spin spirals and isolated skyrmions at low magnetic field exploiting vanishing magnetic anisotropy. *Nat. Commun.* **9**, 1015 (2018).
8. Mathur, N. et al. Electron holography and magnetotransport measurements reveal stabilized magnetic skyrmions in Fe<sub>1-x</sub>Co<sub>x</sub>Si nanowires. *ACS Nano* **13**, 7833–7841 (2019).
9. Stolt, M. J. et al. Electrical detection and magnetic imaging of stabilized magnetic skyrmions in Fe<sub>1-x</sub>Co<sub>x</sub>Ge (x < 0.1) microplates. *Adv. Funct. Mater.* **29**, 1805418 (2019).
10. Mühlbauer, S. et al. Skyrmion lattice in a chiral magnet. *Science* **323**, 915–919 (2009).
11. Yu, X. Z. et al. Real-space observation of a two-dimensional skyrmion crystal. *Nature* **465**, 901–904 (2010).
12. Münzer, W. et al. Skyrmion lattice in the doped semiconductor Fe<sub>1-x</sub>Co<sub>x</sub>Si. *Phys. Rev. B* **81**, 041203(R) (2010).
13. Yu, X. Z. et al. Near room-temperature formation of a skyrmion crystal in thin-films of the helimagnet FeGe. *Nat. Mater.* **10**, 106–109 (2011).
14. Kanazawa, N. et al. Possible skyrmion-lattice ground state in the b20 chiral-lattice magnet mng as seen via small-angle neutron scattering. *Phys. Rev. B* **86**, 134425 (2012).
15. Seki, S., Yu, X. Z., Ishiwata, S. & Tokura, Y. Observation of skyrmions in a multi-ferroic material. *Science* **336**, 198–201 (2012).
16. Milde, P. et al. Unwinding of a skyrmion lattice by magnetic monopoles. *Science* **340**, 1076–1080 (2013).
17. Tanigaki, T. et al. Real-space observation of short-period cubic lattice of skyrmions in MnGe. *Nano Lett.* **15**, 5438–5442 (2015).
18. Qian, F. et al. Phase diagram and magnetic relaxation phenomena in Cu<sub>2</sub>OSeO<sub>3</sub>. *Phys. Rev. B* **94**, 064418 (2016).
19. Pappas, C. et al. Magnetic fluctuations, precursor phenomena, and phase transition in MnSi under a magnetic field. *Phys. Rev. Lett.* **119**, 047203 (2017).
20. Kanazawa, N., Seki, S. & Tokura, Y. Noncentrosymmetric magnets hosting magnetic skyrmions. *Adv. Mater.* **29**, 1603227 (2017).
21. Ishikawa, Y., Tajima, K., Bloch, D. & Roth, M. Helical spin structure in manganese silicide MnSi. *Sol. St. Commun.* **19**, 525–528 (1976).
22. Nakanishi, O., Yanase, A., Hasegawa, A. & Kataoka, M. The origin of the helical spin density wave in MnSi. *Sol. St. Commun.* **35**, 995–998 (1980).
23. Lundgren, L., Beckman, O., Attia, V., Bhattacharjee, S. P. & Richardson, M. Helical spin arrangement in cubic FeGe. *Phys. Scr.* **1**, 69–72 (1970).
24. Siegfried, S.-A. et al. Spin-wave dynamics in the helimagnet FeGe studied by small-angle neutron scattering. *Phys. Rev. B* **95**, 134415 (2017).
25. Skyrme, T. H. A unified field theory of mesons and baryons. *Nucl. Phys.* **31**, 556–569 (1962).
26. Pokrovsky, V. L. Properties of ordered, continuously degenerate systems. *Adv. Phys.* **28**, 595–656 (1979).
27. Bogdanov, A. N. & Yablonskii, D. A. Thermodynamically stable “vortices” in magnetically ordered crystals. The mixed state of magnets. *Sov. Phys. JETP* **68**, 101–103 (1989).
28. Bogdanov, A. & Hubert, A. Thermodynamically stable magnetic vortex states in magnetic crystals. *J. Magn. Magn. Mater.* **138**, 255–269 (1994).
29. Röbber, U. K., Bogdanov, A. N. & Pfeleiderer, C. Spontaneous skyrmion ground states in magnetic metals. *Nature* **442**, 797–801 (2006).
30. Butenko, A. B., Leonov, A. O., Röbber, U. K. & Bogdanov, A. N. Stabilization of skyrmion textures by uniaxial distortions in noncentrosymmetric cubic helimagnets. *Phys. Rev. B* **82**, 052403 (2010).
31. Buhrandt, S. & Fritz, L. Skyrmion lattice phase in three-dimensional chiral magnets from monte carlo simulations. *Phys. Rev. B* **88**, 195137 (2013).
32. Nagaosa, N. & Tokura, Y. Topological properties and dynamics of magnetic skyrmions. *Nat. Nanotechnol.* **8**, 899–911 (2013).
33. Leonov, A. O. & Mostovoy, M. Multiply periodic states and isolated skyrmions in an anisotropic frustrated magnet. *Nat. Commun.* **6**, 8275 (2015).
34. Leonov, A. O. & Bogdanov, A. N. Crossover of skyrmion and helical modulations in noncentrosymmetric ferromagnets. *N. J. Phys.* **20**, 043017 (2018).
35. Leonov, A. O. & Pappas, C. Skyrmion clusters and conical droplets in bulk helimagnets with cubic anisotropy. *Phys. Rev. B* **99**, 144410 (2019).
36. Leonov, A. O., Pappas, C. & Kézsmárki, I. Field and anisotropy driven transformations of spin spirals in cubic skyrmion hosts. *Phys. Rev. Res.* **2**, 043386 (2020).
37. Karube, K. et al. Robust metastable skyrmions and their triangular-square lattice structural transition in a high-temperature chiral magnet. *Nat. Mater.* **15**, 1237–1242 (2016).
38. Morikawa, D. et al. Deformation of topologically-protected supercooled skyrmions in a thin plate of chiral magnet Co<sub>8</sub>Zn<sub>8</sub>Mn<sub>4</sub>. *Nano Lett.* **17**, 1637–1641 (2017).
39. Chacon, A. et al. Observation of two independent skyrmion phases in a chiral magnetic material. *Nat. Phys.* **14**, 936–941 (2018).
40. Quian, F. et al. New magnetic phase of the chiral skyrmion material Cu<sub>2</sub>OSeO<sub>3</sub>. *Sci. Adv.* **4**, eaat7323 (2018).
41. Halder, M. et al. Thermodynamic evidence of a second skyrmion lattice phase and tilted conical phase in Cu<sub>2</sub>OSeO<sub>3</sub>. *Phys. Rev. B* **98**, 144429 (2018).
42. Lin, S.-Z., Saxena, A. & Batista, C. D. Skyrmion fractionalization and merons in chiral magnets with easy-plane anisotropy. *Phys. Rev. B* **91**, 224407 (2015).
43. Kézsmárki, I. et al. Néel-type skyrmion lattice with confined orientation in the polar magnetic semiconductor GaV<sub>4</sub>S<sub>8</sub>. *Nat. Mater.* **14**, 1116–1122 (2015).
44. Nayak, A. K. et al. Magnetic antiskyrmions above room temperature in tetragonal heusler materials. *Nature* **548**, 561–566 (2017).
45. Bordács, S. et al. Equilibrium skyrmion lattice ground state in a polar easy-plane magnet. *Sci. Rep.* **7**, 7584 (2017).
46. Leonov, A. O. & Kézsmárki, I. Skyrmion robustness in noncentrosymmetric magnets with axial symmetry: The role of anisotropy and tilted magnetic fields. *Phys. Rev. B* **96**, 214413 (2017).
47. Ehlers, D. et al. Exchange anisotropy in the skyrmion host GaV<sub>4</sub>S<sub>8</sub>. *J. Phys.: Condens. Matter* **29**, 065803 (2016).
48. Butykai, A. et al. Squeezing magnetic modulations by enhanced spin-orbit coupling of 4d electrons in the polar semiconductor GaMo<sub>4</sub>S<sub>8</sub>. Preprint at <https://arxiv.org/abs/1910.11523> (2019).
49. Geirhos, K. et al. Macroscopic manifestation of domain-wall magnetism and magnetoelectric effect in a Néel-type skyrmion host. *npj Quantum Mater.* **5**, 44 (2020).
50. Gross, B. et al. Stability of Néel-type skyrmion lattice against oblique magnetic fields in GaV<sub>4</sub>S<sub>8</sub> and GaV<sub>4</sub>Se<sub>8</sub>. *Phys. Rev. B* **102**, 104407 (2020).
51. Hori, T., Shiraishi, H. & Ishii, Y. Magnetic properties of β-mncozn alloys. *J. Magn. Mater.* **310**, 1820–1822 (2007).
52. Tokunaga, Y. et al. A new class of chiral materials hosting magnetic skyrmions beyond room temperature. *Nat. Commun.* **6**, 7638 (2015).
53. Yu, X. Z. et al. Transformation between meron and skyrmion topological spin textures in a chiral magnet. *Nature* **564**, 95–98 (2018).
54. Karube, K. et al. Metastable skyrmion lattices governed by magnetic disorder and anisotropy in β-mn-type chiral magnets. *Phys. Rev. B* **102**, 064408 (2020).
55. Nagase, T. et al. Smectic liquid-crystalline structure of skyrmions in chiral magnet Co<sub>8.5</sub>Zn<sub>7.5</sub>Mn<sub>4</sub>(110) thin film. *Phys. Rev. Lett.* **123**, 137203 (2019).
56. Nagase, T. et al. Observation of domain wall skyrmions in chiral magnets. *Nat. Commun.* **12**, 3490 (2021).
57. Karube, K. et al. Skyrmion formation in a bulk chiral magnet at zero magnetic field and above room temperature. *Phys. Rev. Mat.* **1**, 074405 (2017).
58. Karube, K. et al. Disordered skyrmion phase stabilized by magnetic frustration in a chiral magnet. *Sci. Adv.* **4**, eaar7043 (2018).
59. Maleyev, S. V. Cubic magnets with Dzyaloshinskii-Moriya interaction at low temperature. *Phys. Rev. B* **73**, 174402 (2006).
60. Ukleev, V. et al. Element-specific soft x-ray spectroscopy, scattering, and imaging studies of the skyrmion-hosting compound Co<sub>8</sub>Zn<sub>8</sub>Mn<sub>4</sub>. *Phys. Rev. B* **99**, 144408 (2019).
61. Nakajima, T. et al. Correlation between site occupancies and spin-glass transition in skyrmion host Co<sub>10-x/2</sub>Zn<sub>10-x/2</sub>Mn<sub>x</sub>. *Phys. Rev. B* **100**, 064407 (2019).
62. Ford, P. J. & Mydosh, J. A. Electrical resistivity of noble-metal-host-3d solute spin-glass alloys. *Phys. Rev. B* **14**, 2057–2070 (1976).
63. Kindervater, J. et al. Evolution of magnetocrystalline anisotropies in Mn<sub>1-x</sub>Fe<sub>x</sub>Si and Mn<sub>1-x</sub>Co<sub>x</sub>Si as inferred from small-angle neutron scattering and bulk properties. *Phys. Rev. B* **101**, 104406 (2020).
64. Bocarsly, J. D., Heikes, C., Brown, C. M., Wilson, S. D. & Seshadri, R. Deciphering structural and magnetic disorder in the chiral skyrmion host materials Co<sub>x</sub>Zn<sub>y</sub>Mn<sub>z</sub>(x + y + z = 20). *Phys. Rev. Mater.* **3**, 014402 (2019).
65. Stasinopoulos, I. et al. Low spin wave damping in the insulating chiral magnet Cu<sub>2</sub>OSeO<sub>3</sub>. *Appl. Phys. Lett.* **111**, 032408 (2017).
66. Landau, L. D. & Lifshitz, E. M. On the theory of the dispersion of magnetic permeability in ferromagnetic bodies. *Phys. Z. Sowj.* **8**, 153–169 (1935).
67. Gilbert, T. L. A lagrangian formulation of the gyromagnetic equation of the magnetization field. *Phys. Rev.* **100**, 1243 (1955).
68. Kittel, C. Interpretation of anomalous larmor frequencies in ferromagnetic resonance experiment. *Phys. Rev.* **71**, 270 (1947).
69. Kittel, C. Ferromagnetic resonance. *J. Phys. Radium* **12**, 291–302 (1951).
70. Tannenwald, P. E. *IRE WESCON Convention Record*, Vol. 3, Ch. 1, 134 (Institute of Radio Engineers, Inc., 1959).
71. Morrish, A. H. *The Physical Principles of Magnetism*, Ch. 10, 556–559, (John Wiley & Sons, Inc., 1965).



72. Smit, J. & Beliers, H. G. Ferromagnetic resonance absorption in  $\text{BaFe}_{12}\text{O}_{19}$ . *Philips Res. Rep.* **10**, 113 (1955).
73. Suhl, H. Ferromagnetic resonance in nickel ferrite between one and two kilomegacycles. *Phys. Rev.* **97**, 555 (1955).

## ACKNOWLEDGEMENTS

We are grateful to V. Tsurkan, D. Vieweg and V. Fritsch for their technical assistance. This research was supported by the German Research Foundation (DFG) via the Priority Program SPP2137, Skyrmionics, under Grant Nos. KE 2370/1-1 and by the Japanese Government via the JSPS Grant-in-Aids for Scientific Research (Grant No. 20K15164).

## AUTHOR CONTRIBUTIONS

M.P., D.E., B.S. and H.-A. K.v.N. performed and analysed the FMR measurements. J.S.W., V.U. and K.K. performed and analysed the SANS measurements. K.K., A.K., Y. Tokunaga and Y. Taguchi grew the crystals. All authors discussed the content of the manuscript. M.P. and I.K. wrote the manuscript. I.K. planned and supervised the project.

## FUNDING

Open Access funding enabled and organized by Projekt DEAL.

## COMPETING INTERESTS

The authors declare no competing interests.

## ADDITIONAL INFORMATION

**Supplementary information** The online version contains supplementary material available at <https://doi.org/10.1038/s41535-021-00365-y>.

**Correspondence** and requests for materials should be addressed to M.P.

**Reprints and permission information** is available at <http://www.nature.com/reprints>

**Publisher's note** Springer Nature remains neutral with regard to jurisdictional claims in published maps and institutional affiliations.



**Open Access** This article is licensed under a Creative Commons Attribution 4.0 International License, which permits use, sharing, adaptation, distribution and reproduction in any medium or format, as long as you give appropriate credit to the original author(s) and the source, provide a link to the Creative Commons license, and indicate if changes were made. The images or other third party material in this article are included in the article's Creative Commons license, unless indicated otherwise in a credit line to the material. If material is not included in the article's Creative Commons license and your intended use is not permitted by statutory regulation or exceeds the permitted use, you will need to obtain permission directly from the copyright holder. To view a copy of this license, visit <http://creativecommons.org/licenses/by/4.0/>.

© The Author(s) 2021